Wavefront Reconstruction by its Slopes via Physics-Informed Neural Networks

T.E. Romanenko[1], A.V. Razgulin[2], N.G. Iroshnikov[3], A.V. Larichev[4]

[1] MSU, Faculty of Computational Mathematics and Cybernetics, 119991 Moscow, Russia - romanenko@cs.msu.ru
[2] MSU, Faculty of Computational Mathematics and Cybernetics, 119991 Moscow, Russia - razgulin@cs.msu.ru
[3] MSU, Faculty of Physics, 119234 Moscow, Russia - nikita@optics.ru
[4] MSU, Faculty of Physics, 119234 Moscow, Russia - larichev@optics.ru

Keywords: Wavefront Slope, Physics-Informed Neural Networks, Shack–Hartmann sensor.

Abstract

The problem of wavefront reconstruction by its slopes, related to the the phase recovery of a light wave based on Shack-Hartmann sensor data, is considered. A reconstruction method based on the application of physics-informed neural networks to slope measurement data on both regular and irregular grids in two modifications WRPINN and WRRADPINN is proposed. A comparison with the reconstruction method based on the variational approach combined with the projection method using a fractional smoothness stabilizer on typical smooth, nonsmooth, and discontinuous wavefronts defined on a regular grid is given. The results of the method's performance on irregular grids and with partially missing data are analyzed, leading to the conclusion about its effectiveness in handling such data.

1. Introduction

The problem of wavefront reconstruction from the data of its local slopes is one of the important problems arising in many applications: in the estimation of atmospheric turbulence parameters (Andreeva et al., 2012), in the restoration of the light wave phase for the purposes of adaptive optics (Larichev et al., 2002), in various applied problems of medical physics (Baryshnikov et al., 2019), (Goncharov et al., 2015), and others. In particular, multifocal intraocular lenses (IOLs) have recently been implanted in an increasing number of patients to correct refractive anomalies. However, multifocal IOLs can lead to undesirable visual artifacts, as well as make it difficult to achieve a clear and wide view of the retina during ophthalmoscopy and visualization by optical methods. To solve these problems, it is necessary to develop special mathematical methods for the reconstruction of nonsmooth wavefronts from measured slopes, which will allow visualization and subsequent analysis of the optical image of human retinal structures in vivo.

The mathematical formulation of the problem consists in restoring the function of two variables by measurements of its partial derivatives of these variables. The peculiarity of the problem under consideration is that both the slope data (due to distortions of various nature arising during measurements) and the wavefronts themselves (e.g., IOL) are often nonsmooth and even discontinuous, which makes the development of stable methods for wavefront reconstruction an urgent task that attracts the attention of specialists (see, e.g., (Liu et al., 2024), (Gu et al., 2021), (Huang et al., 2023)). Such spiral vortex structures are one of the frequently studied phenomena both in atmospheric turbulence (Wang et al., 2023), (Hyde and Spencer, 2023) and in the case of laser beams (Hyde and Porras, 2023), (Acevedo et al., 2023), (Kozlova et al., 2024).

It is also worth noting that, given the specific nature of the Shack-Hartmann sensor, the task of analyzing and reconstructing the wavefront is invariably faced, both from data specified inaccurately in the case when the amplitude is comparable to the amount of the noise recorded at the sensors, and in the case when data are missing in the region of several sub-apertures. Moreover, from the point of view of higher resolution wavefront reconstruction, it is worth keeping a balance between increasing resolution by increasing the number of sub-apertures and the fact that increasing the number of sub-apertures too much can cause the total intensity within each sub-aperture to drop to values comparable to the noise on the sensors. This leads to additional difficulties in using the existing methods due to a number of limitations imposed by them on the grid on which the slope data are specified and its resolution.

In (Razgulin et al., 2017), a finite-dimensional variational-projection scheme aimed at reconstructing a nonsmooth wavefront is considered. In (Razgulin et al., 2019)), a family of new wavefront reconstructors is proposed, in which a stabilizer with fractional second-order difference derivatives is added to improve the spatial-frequency response of the scheme and its alignment at high frequencies. In (Razgulin et al., 2022), under the condition of matching the grid step with the stabilizer parameters, estimates of the accuracy of the method (Razgulin et al., 2019) are obtained from anisotropic Sobolev spaces with fractional smoothness indices. The results of these works show the effectiveness of the proposed variational-projection method for the problems of reconstructing nonsmooth wavefronts defined on rectangular regions and when uniform grides are chosen for each variable. However, adapting the projection method to more general domains (including unconnected ones) and non-uniform grids given by the original measurement data arising in applications greatly complicates its implementation and reduces its efficiency. In these cases, a possible alternative is the use of machine learning methods and neural networks.

Recently, there has been significant development in the field related to wavefront reconstruction in various applications using deep learning(Wang et al., 2024), which includes the application of various neural network architectures. One popular approach is based on recovering the Zernike coefficients of the recorded wavefront from data obtained directly from a Shack-Hartmann sensor using modifications of various convolutional networks that have been shown to be effective in re-

This contribution has been peer-reviewed.
https://doi.org/10.5194/isprs-archives-XLVIII-2-W9-2025-233-2025

gression problems, especially ResNet (Gu et al., 2021), (He et al., 2021), (Ning et al., 2024), as well as using Self-Attention blocks embedded in convolutional network modules (Ge et al., 2023), (Zhang et al., 2024). Another popular approach is to use modifications of convolutional networks no longer applied to regression problems, but to the reconstruction of two-dimensional datasets, typically images. In (Zheng et al., 2024), a U-Net-type convolutional network is considered to recover a high-resolution wavefront directly from its low-resolution version, while in (Zhao et al., 2022), the focus is on reconstructing slopes in all sub-apertures of the considered region using slope information from only a limited number of sub-apertures. It is also worth noting that the application of deep learning to wavefront reconstruction is not limited to a purely software solution (Platt and Shack, 2001), (Zhao et al., 2022), (Zhang et al., 2024), (Ning et al., 2024), (Ma et al., 2023), (Ge et al., 2023), (Gu et al., 2021), (Wu et al., 2023b), but also includes more complex hardware and software versions (Zheng et al., 2024), (Grose et al., 2024), including, for example, an event-based camera operating in synchronization with a standard frame-based version (Grose et al., 2024). Nevertheless, the approach based on the application of convolutional neural networks for wavefront reconstruction is used not only to work with data obtained from the Shack-Hartmann sensor, but also successfully applied to the reconstruction of the Zernike coefficients, which define the desired wavefront, from the analysis of a pair of images consisting of an image in focus and its defocused version (Ge et al., 2023), (Ma et al., 2023).

In this regard, the approach based on the application of physics-informed neural networks (PINN) to solve initial boundary value problems for partial derivative equations (Raissi et al., 2019), which has been gaining popularity in the last few years, looks promising. The approach is based on the ability of virtually any modern framework (PyTorch, TensorFlow, JAX) implementing machine learning methods to analytically specify a nonlinear approximation of the desired function and compute its derivatives as well. This possibility allows us to reduce the initial boundary value problem for the partial derivative equation to the problem of minimizing a functional containing the deviations of this nonlinear approximation from the initial boundary data and its residual when substituted into the equation under consideration. The proposed approach is not limited by the specific resolution or location of the points at which the slope data were obtained, or by the requirement that they be uniformly located. This allows, when applied to the problem considered in this paper, wavefront reconstruction to be performed on both uniformly specified and arbitrary grids. Moreover, the application of this approach is possible for the case of regions for which there is no information in a part of points or in a set of subareas or for the case when the slopes are known in a relatively small number of points and it is required to reconstruct the wavefront of a significantly higher resolution. The proposed method was evaluated on typical wavefronts encountered in ophthalmological applications, turbulent distortion correction and optical quantum communication.

2. Problem statement

In this paper, we propose to reconstruct the wavefront $u(x, y)$ from measurements of its slopes $g_1(x, y)$, $g_2(x, y)$ along the corresponding x and y directions by considering the corresponding problem of minimizing the total deviation of the slopes of the sought nonlinear approximation from the known values in a given set of points. The reconstruction problem is generally considered within an arbitrary aperture, but a comparison with the projection method is made for the case of a square aperture $\Omega = [-\pi, \pi] \times [-\pi, \pi]$ or a normalized square aperture $\Omega_0 = [-1.0, 1.0] \times [-1.0, 1.0]$ containing a unit circle, in which the Zernike polynomialsthat are typical for describing wavefronts of ophthalmological nature and atmospheric wavefronts are defined.

3. Method of wavefront reconstruction by physics-informed neural network

3.1 Neural network approximation

The method proposed in this paper is based on approximating the reconstructed wavefront by a nonlinear approximation given by a fully-connected neural network

$$\begin{aligned} u = u(\mathbf{x}, \boldsymbol{\theta}) &= \sigma^{(L)} \left(\frac{1}{n_{L-1}} W^{(L)} y^{(L-1)} + b^{(L)} \right), \\ y^{(l)} &= \sigma^{(l)} \left(\frac{1}{n_{l-1}} W^{(k)} y^{(l-1)} + b^{(l)} \right). \end{aligned} \tag{1}$$

Here $\mathbf{x} = (x, y) \in \Omega$ is the input coordinate vector, $\sigma^{(l)} : \mathbb{R} \to \mathbb{R}$ is the piecewise nonlinear activation function, $y^{(l)} \in \mathbb{R}^{n_l}$ — hidden layer with neurons, $y^{(0)} = \mathbf{x}$, $W^{(l)} \in \mathbb{R}^{n_l \times n_{l-1}}$, $b^{(l)} \in \mathbb{R}^{n_l}$, $\boldsymbol{\theta} = \{W^{(i)}, b^{(i)}, i = \overline{(1, L)}\}$ is the vector of weights obtained during the solution of the minimization problem, $l = \overline{1, L-1}$.

As an activation function $\sigma^{(i)}$ in problems of recovering solutions of initial boundary value problems for partial derivative equations, as a rule, $\tanh(\cdot)$ —hyperbolic tangent and trigonometric $\sin(\cdot)$ are considered. Unlike projective constructions based on finite elements of fixed shape, the method gives a smooth nonlinear approximation and does not require a priori any special structure of the Ω domain.

3.2 PINN minimization problem

In general, to find the weights of the desired approximation $u(\mathbf{x}, \boldsymbol{\theta})$ we consider the problem of minimizing the functional

$$L(\boldsymbol{\theta}) = L_b(\boldsymbol{\theta}) + L_r(\boldsymbol{\theta}) \to \min, \tag{2}$$

where $L_r(\boldsymbol{\theta})$ is the component responsible for minimizing the residual with the registered slopes $g_1(x, y)$, $g_2(x, y)$, given by the formula

$$\begin{aligned} L_r(\boldsymbol{\theta}) = \frac{1}{N_r} \sum_{i=1}^{N_r} \Bigg\{ &\left(u_x(\mathbf{x}_r^{(i)}, \boldsymbol{\theta}) - g_1(\mathbf{x}_r^{(i)}) \right)^2 + \\ &\left(u_y(\mathbf{x}_r^{(i)}, \boldsymbol{\theta}) - g_2(\mathbf{x}_r^{(i)}) \right)^2 \Bigg\} \end{aligned} \tag{3}$$

and $L_b(\boldsymbol{\theta}) = \frac{1}{N_b} \sum_{i=1}^{N_b} \left(u(\mathbf{x}_b^{(i)}, \boldsymbol{\theta}) - g_b(\mathbf{x}_b^{(i)}) \right)^2$ is the component minimizing the deviation from the boundary values given at the given boundary points $\mathbf{x}_b^{(i)}$, $i = \overline{1, N_b}$ by some known function $g_b(\mathbf{x})$.

In the case of typical problems of wavefront reconstruction by slopes in the absence of a priori information about the behavior of the wavefront on the boundary, the value $L_b(\boldsymbol{\theta})$ is not included in (2) and further in the paper we will consider the version that does not take into account the contribution of values on the boundary of the region. For each function with predefined slopes on a grid to be recovered, the training data consisted solely of slope values, while the learning process comprised solving the minimization problem for functional L_r.

The choice of the N_r points used to minimize (2) depends on the domain and can be either a regular uniform rectangular grid $\mathbf{x}_b^{(i)} = (x_k, y_j)$, $x_k = x_{min} + k \cdot h_x, y_j = y_{min} + j \cdot h_y$, $k = \overline{(1, N_x)}, j = \overline{(1, N_y)}$ or some given set of points $\mathbf{x}_b^{(i)} = (x_i, y_i) \in \Omega, i = \overline{(1, N_r)}$, such as those obtained by computing the slopes in the Shack-Hartmann sensor.

3.3 RADPINN minimization problem

It is worth noting that, despite the efficiency demonstrated by classical PINNs in solving initial boundary value problems, there are a number of drawbacks that numerous modifications of the classical approach are aimed at correcting. Without claiming completeness of the given directions for improvement and proposed methods, let us mention the problem of modeling a rapidly oscillating solution (Wu et al., 2023a), (Wang et al., 2022), which is of the greatest interest in the context of the considered problem of wavefront restoration. A significant number of papers present examples in which the solution is a relatively rapidly oscillating function, when modeling which the classical PINN approach often shows a significant deviation from the exact solution, see for example (Wang et al., 2022). Despite the existence of a wide set of proposed methods for modifying both the nonlinear approximation of the solution itself, the choice of the set of points at which the minimized discrepancy is computed, and the minimization algorithm, it is worth considering their limitations and complexity of application in the case of the specificity of the problem of recovering a function from its slopes. One promising approach (Wu et al., 2023a) proposes several modifications of the algorithm for constructing the minimized functional and the set of points used to compute it. In the case where we are restricted to a fixed location of points on the plane where the slopes of the wavefront to be reconstructed are known, we can use the RADPINN modification, in which the functional changes every M iterations at each step is represented by the formula:

$$L_r^{(j)}(\boldsymbol{\theta}) = \frac{1}{N_r} \sum_{\mathbf{x} \in X_j}^{N_r} \Bigg\{ (u_x(\mathbf{x}, \boldsymbol{\theta}) - g_1(\mathbf{x}))^2 + (u_y(\mathbf{x}, \boldsymbol{\theta}) - g_2(\mathbf{x})^2 \Bigg\},$$

where $X_j = \left\{\mathbf{x} \in \{x_r^{(i)}, i = \overline{1, N_r}\}\right\}$ is the set of points $\mathbf{x}$, selected according to the corresponding probability distribution, which takes into account the magnitude of the quadratic deviation of the derivatives from the slopes measured at the point.

In the following, the modifications of the method discussed in sections 3.2 and 3.3 will be referred to as WRPINN and WRRADPINN, respectively, indicating, if necessary, the activation function σ chosen for implementation in the neural network approximation (1) in parentheses after the name.

3.4 Program implementation

In terms of the used software framework it is possible to use any machine learning framework that contains the capabilities of analytical differentiation of the desired nonlinear approximation given by the neural network by its input and parameters. In this work, the Python language PyTorch machine learning framework was used. The software implementation is provided on the open web service GitHub (Romanenko, 2025). To test the performance and compare the running time of the presented method with existing analogs, a MacBook Pro 14 laptop with an Apple M3 Max processor with 14 processor cores and 30 graphics cores and a computer with an AMD Ryzen 9 5900X processor and NVIDIA RTX 3080 Ti GPU were used. The stochastic Adam optimizeror its combination with a memory-constrained modification of the L-BFGS quasi-Newton method was used as the weight parameters optimizer.

4. Data description

With important medical applications in mind, testing of the method was performed on wavefronts characteristic of distortions that occur in the optical system of the human eye and can be described using Zernike polynomials, and a class of nonsmooth and discontinuous spiral wavefronts used in IOL modeling (Kolodziejczyk et al., 2007).

4.1 Wavefronts

4.1.1 Zernike polynomials One of the important types of wavefronts, typical also for ophthalmologic applications, is the front defined by orthogonal Zernike polynomials in the unit circle $Z_n^m(\rho, \varphi) = R_n^m(\rho)\cos(m\varphi)$ and $Z_n^{-m}(\rho, \varphi) = R_n^m(\rho)\sin(m\varphi)$, where the radial polynomials are defined by the formula $R_n^m(\rho) = \sum_{k=0}^{(n-m)/2} \frac{(-1)^k (n-k)!}{k!(\frac{n+m}{2}-k)!(\frac{n-m}{2}-k)!}\rho^{n-2k}$.An example of such a polynomial $Z(13, 3)$ multiplied by a super-Gaussian function is shown in part a) of Figure 1.

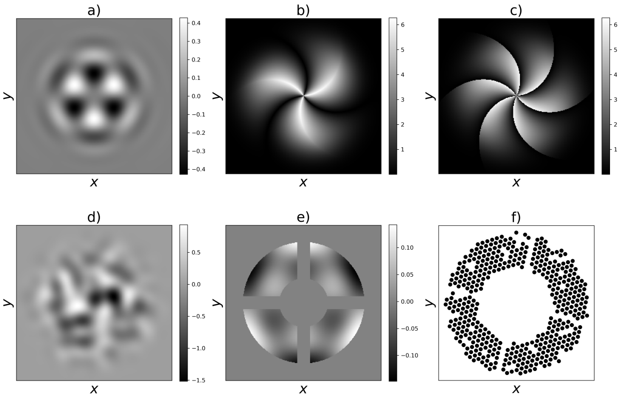

Figure 1. Examples of the considered wavefronts.

4.1.2 Wavefronts of atmospheric distortions A Butterworth filter (see, e.g., (Razgulin et al., 2017)) with a selected pass frequency superimposed on the noise image given by Gaussian or Poisson noise (see Figure 1 part d)) was used as a wavefront typical of atmospheric distortion.

4.1.3 Non-smooth and discontinuous spiral wavefronts Given the relevance of the reconstruction of different spiral wavefronts (Hyde and Porras, 2023), (Acevedo et al., 2023) (Wang et al., 2023), (Hyde and Spencer, 2023), (Kozlova et al., 2024), the following types of such fronts were considered: non-smooth and discontinuous. As a non-smooth wavefront, a front defined by the surface $u(\rho, \varphi, n, \varkappa) = u_0 + \exp\left\{-(\rho/a)^{2M}\right\} \cdot U(\rho, \varphi, n, \varkappa)$ was chosen. Here $\zeta = \varkappa r + 2n(\varphi - \pi/2) + \pi/6$, $U(\rho, \varphi, n, \varkappa) = \zeta \mod 2\pi$, if $\left[\frac{\zeta}{2\pi}\right]$ is odd, and $2\pi - \zeta \mod 2\pi$ otherwise, $n \in \mathbb{N}$, $\varkappa \in \mathbb{R}$.

Since the wavefront phase can experience a $2\pi n$ discontinuity in the case of points with field amplitude equal to 0, such as when propagating through a turbulent medium (Gbur and Tyson, 2008)), the slopes of the wavefront in the discontinuity zone are not determined. Therefore, a model surface given by the formula above,where the function $U(\rho, \varphi, n, \varkappa)$ characterizes the discontinuity in the angular variable: $U(\rho, \varphi, n, \varkappa) = (\varkappa r + 2n(\varphi - \pi/2) + \pi/6) \mod 2\pi$.

Examples of the wavefronts described in subsection 4.1.3 are shown in Figure 1 in parts b) and c).

4.2 Irregular grid

It is worth noting that, in addition to the specifics of the data presented in the previous sections, it is important to take into account the specifics of the region on which the Shack-Hartmann tilts are recorded. Often in applications, the region is a circular aperture on which, in addition to ”bad” regions or regions with amplitude values below some threshold under consideration, there may be several band-like regions where data are not available for registration. An example of such a region with a characteristic arrangement of points where slope data are recorded and regions where no slope information is available, as well as an example of a wavefront defined on an annular aperture with excluded band-like regions, are shown in Figure 1 parts (f) and (e), respectively.

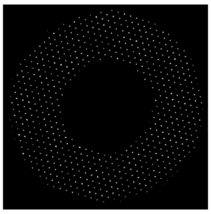

Figure 2. Example of data obtained directly from the Shack-Hartmann sensor of the setup (Kopylov et al., 2024).

A typical example of the location of the points and the experimental data themselves, recorded directly by the Shack-Hartmann sensor mounted on the telescope (Kopylov et al., 2024), from which the slopes are subsequently calculated, is shown in Figure 2. Note that the characteristic number of points in this case is 2 orders (400-500 times) smaller than in the case of the uniform grid considered earlier.

5. Results for regular grids

Comparison of the accuracy results of the presented method with the variational-projection method was carried out on regular grids of size $N \times N$, $N = 126, 256, 512, 1024, 2048$ on Zernike polynomials, non-smooth and discontinuous spiral fronts and atmospheric fronts described in sections 4.1.1-4.1.3. The following examples show the results on a regular grid for $N = 256$. All calculations were performed for slope values to which Poisson noise was added, with a magnitude of approximately 2% of the amplitude. The number of iterations of the presented method depending on the modification was chosen so that the running time of all modifications was close. All fronts are considered in the region $\Omega = [-\pi, \pi] \times [-\pi, \pi]$. In all images of the results presented below, the left image in the row corresponds to the original analytically specified wavefront plotted on the corresponding grid section, the center image corresponds to the one reconstructed by the specified method and plotted on the specified grid, and the right image corresponds to the absolute deviation of the reconstructed front from the original one.

5.1 Comparison with the variational-projection method

As a preliminary part of the analysis of the method performance quality, we compared the variational-projection method with 4 different modifications: WRPINN and WRRADPINN, in which $\tanh$ and $\sin$ were chosen as the activation function. For each of the considered examples, to which the variational-projection method is applicable, for it and for all 4 modifications, the table presents the results of recovery quality by 3 metrics: relative standard deviation MSE_N, structural similarity index $SSIM$ and percentage error $\delta_{perc} = \dfrac{\max|z_e - z_r|}{\max z_e - \min z_e} \cdot 100\%$, where $z_e(x, y)$ is the exact value of the front, $z_r(x, y)$ is the reconstructed value of the front, and $\max$ and $\min$ are taken over the whole Ω region.

In all images presented in Section 5.1 (a), (d) correspond to the original analytically specified wavefront; (b) — to the front reconstructed by the variational-projection method, (e) — to the front reconstructed by the specified modification of the PINN method; (c) — to the absolute deviation of the front reconstructed by the variational-projection method from the original front; (f) — to the absolute deviation of the front reconstructed by the specified modification of the PINN method from the original front.

5.1.1 Zernike polynomials In the case of low-order Zernike polynomials, all 4 modifications of the proposed method produce qualitatively similar results, as reflected in Table 1. Typical results of the reconstruction of smooth low-frequency surfaces given by the $Z(5, 3)$ Zernike polynomial by the variational-projection method (top row) and WRRADPINN($\tanh$) method (bottom row) are presented in Figure3.

Method	MSE_N	δ_{perc}	SSIM
Projection	0.0014	0.010%	0.999
WRPINN(tanh)	0.0055	0.33%	0.998
WRPINN(sin)	0.0110	0.54%	0.988
WRRADPINN(tanh)	0.0043	0.21%	0.999
WRRADPINN(sin)	0.0050	0.28%	0.998

Table 1. Accuracy of the methods on the surface given by the Zernike polynomial $Z(5, 3)$.

In the case of a linear combination of higher-order Zernike polynomials $Z(45, 17) - Z(31, -23) + Z(32, -14) - Z(46, 32)$, we observe a situation in which the basic version of the PINN method cannot recover a function characterized by a fast spatial change without additional modifications to the method. Such a situation and the proposed ways to solve it for initial boundary

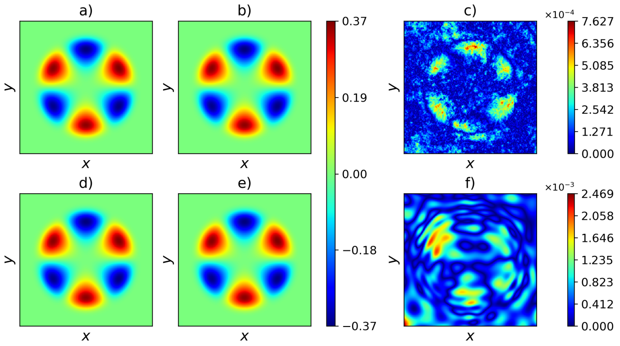

Figure 3. Result of wavefront reconstruction given by the Zernike polynomial $Z(5,3)$.

Method	MSE_N	δ_{perc}	SSIM
Projection	0.0245	1.192%	0.996
WRPINN(tanh)	1.000	50.03%	0.015
WRPINN(sin)	1.0000	50.05%	0.006
WRPINN(sin) ×4 it.	0.1115	7.92%	0.844
WRRADPINN(tanh)	0.2436	19.42%	0.611
WRRADPINN(sin)	0.0752	3.83%	0.901

Table 2. Accuracy of the methods on a surface given by a linear combination of Zernike polynomials.

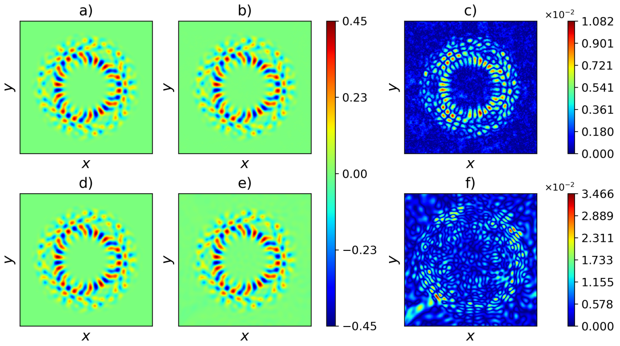

Figure 4. Result of wavefront reconstruction given by a linear combination of Zernike polynomials.

value problems for partial derivative equations are given, for example, in (Wang et al., 2022), (Wu et al., 2023a).

Thus, the WRRADPINN(tanh) modification showed results comparable to the variational-projection method, and the modification of the WRRADPINN(sin) in general produced values close in accuracy. It is also worth noting that in this case the basic version of WRPINN(sin) with a 4-times increase in the number of iterations of the method (and, consequently, the running time) allows us to obtain a relatively good quality of reconstruction. The results of reconstruction of the above surface by the variational-projection (top row) and WRRADPINN(sin) methods (bottom row) are presented in Figure 4.

5.1.2 Spiral wavefronts The comparative values of the accuracy of the modification for a non-smooth spiral wavefront are summarized in Table 3. Despite the best value of the $SSIM$ metric on the WRRADPINN(sin) version, the lowest deviation is characterized by the WRPINN(tanh) modification, the results of which (bottom row) in comparison with the variational-projection method (top row) are presented in Figure 5.

Method	MSE_N	δ_{perc}	SSIM
Projection	0.0406	28.55%	0.993
WRPINN(tanh)	0.0649	22.49%	0.952
WRPINN(sin)	0.0448	39.24%	0.977
WRRADPINN(tanh)	0.0763	33.94%	0.947
WRRADPINN(sin)	0.0483	40.96%	0.975

Table 3. Accuracy of the methods on a non-smooth wavefront.

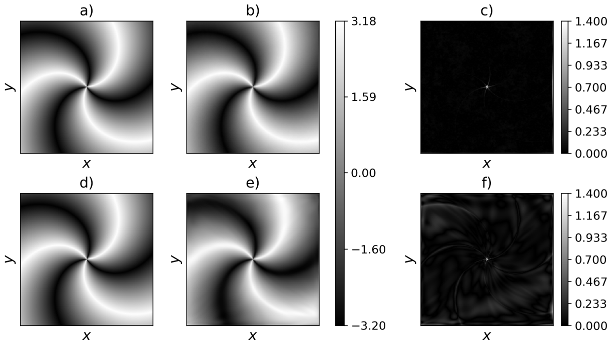

Figure 5. Result of reconstructing a non-smooth spiral wavefront.

The results for the reconstruction of the discontinuous spiral wavefront are presented in Table 4 and for the cases of the variational-projection method (top row) and WRPINN(sin) (bottom row) in Figure 6, respectively. The method is able to give comparable recovery quality, but in the case of discontinuous data, due to the inherently continuous nature of the chosen nonlinear approximation, it loses to the variational-projection method.

Method	MSE_N	δ_{perc}	SSIM
Projection	0.1529	41.58%	0.966
WRPINN(tanh)	0.6136	101.2%	0.611
WRPINN(sin)	0.2797	68.46%	0.802
WRRADPINN(tanh)	0.6547	89.55%	0.561
WRRADPINN(sin)	0.2834	68.71%	0.774

Table 4. Accuracy of the methods on a discontinuous spiral wavefront.

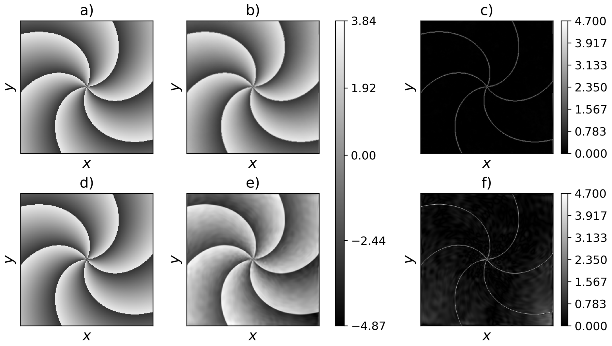

Figure 6. Result of reconstructing a discontinuous spiral wavefront.

5.1.3 Atmospheric wavefronts Simulations for the case of a wavefront characterizing atmospheric turbulence were carried out on wavefronts specified by a Butterworth filter applied to the generated normal distribution. The results of the reconstruction by the variational-projection method (top row) and WRRADPINN(sin) method (bottom row) are presented in Figure 7. In the case of sufficiently high-frequency data, as in the case of high-order Zernike polynomials, the basic version of WRPINN does not allow to recover the desired front with sufficient accuracy, whereas the WRRADPINN modification, especially with the activation function $\sin$, shows a comparatively better quality of recovery.

Method	MSE_N	δ_{perc}	SSIM
Projection	0.0445	2.533%	0.993
WRPINN(tanh)	0.7752	48.56%	0.357
WRPINN(sin)	0.3347	10.61%	0.511
WRRADPINN(tanh)	0.7291	34.09%	0.335
WRRADPINN(sin)	0.2658	9.369%	0.624

Table 5. Accuracy of the methods on the atmospheric wavefront.

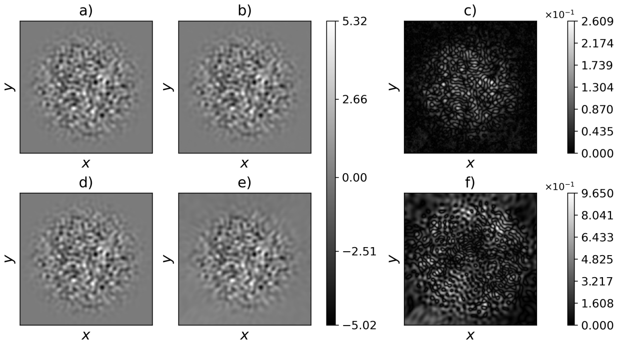

Figure 7. Result of atmospheric wavefront reconstruction.

It should be noted that, in spite of the restoration results presented above, which showed accuracy close to the results obtained with the variational-projection method, the typical runtime of the method on a grid of similar size was more than an order longer on the same hardware and software. This makes the use of the method in cases where the desired front needs to be reconstructed almost in real time currently inefficient given the existing capabilities of modern graphics processing units.

5.2 Results for regular grids with "bad" regions and grids of lower dimensionality

In this section we present the results of the method on those regular domains, the work on which is difficult or impossible for classical methods.

5.2.1 Regular grids with "bad" regions In the case of "bad" points or regions, when applying classical methods, including the variational-projection method, the question of obtaining missing values by interpolation arises. In the case of the method of physics- informed neural networks, the missing points are simply not included in the summands of the minimized functional. At the same time, the design of the method (2) allows us to determine the wavefront in all points of the Ω region without any additional post-processing.

Figure 8 shows the results of WRPINN($\tanh$) method reconstruction for non-smooth and WRRADPINN($\tanh$) method reconstruction for discontinuous wavefronts with two and four "bad" slope regions, respectively. The modifications of the methods that showed the best values in the previously mentioned metrics were chosen for visualization; the metric values for these modifications are given in Table 6. The blackened circles in the figures of the original fronts show the regions where the slope values were missing. When obtaining the modulus of the difference between the exact solution and the reconstructed wavefront, the entire region was considered.

Method	MSE_N	δ_{perc}	SSIM
WRPINN(tanh)	0.0246	21.10%	0.994
WRRADPINN(tanh)	0.9474	117.2%	0.491

Table 6. Accuracy of the WRPINN($\tanh$) and WRRADPINN($\tanh$) on non-smooth and discontinuous wavefronts with "bad" slope regions, respectively.

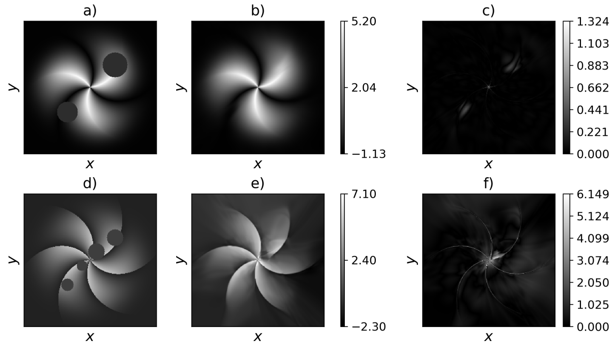

Figure 8. Result of reconstruction of nonsmooth and discontinuous spiral wavefronts with "bad" regions.

The above results show that the method gives good recovery quality under the conditions of location of "bad" regions on both smooth, non-smooth and discontinuous parts of the surface.

5.2.2 Regular grids of lower dimensionality As one example, a grid of smaller (16 times fewer points with slope information than on the original grid) dimensionality was considered and the quality of the reconstruction was tested on it using the variational-projection and PINN methods.

Method	MSE_N	δ_{perc}	SSIM
Projection(tanh)	0.0781	24.20%	0.959
WRRADPINN(tanh)	0.0672	60.36%	0.971

Table 7. Accuracy of the methods for the reduced grid.

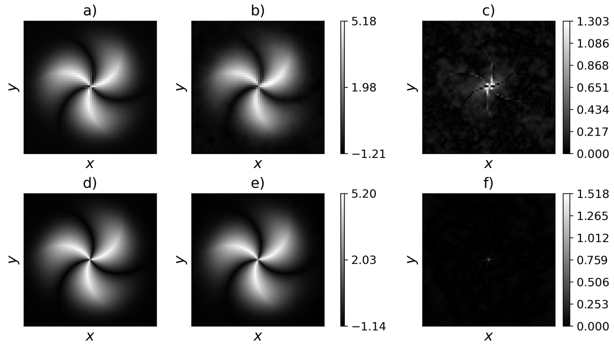

Figure 9. Result of wavefront reconstruction for the reduced grid.

Figure 9 shows the results of wavefront reconstruction from the slopes given on a similar grid reduced by a factor of 16. As can be seen, the proposed method almost completely restored the structure of the wavefront, which is shown by the low value of the absolute deviation from the exact solution on the original, unreduced grid. The emission of the absolute deviation in the central regions is related to the essentially discontinuous nature of the slopes on the reduced grid.

Table 7 shows the values of the reconstruction quality metrics for the variational-projection method, where the comparison was performed on a reduced grid, and for WRRAPINN($\tanh$), for which the comparison was performed on the original size grid. The variational-projection method recovers the desired front with better absolute accuracy, but remains limited to a grid of significantly lower dimensionality.

6. Results for irregular grids

In this section we discuss the results of testing the quality of the method's performance on two types of irregular grids.

6.1 Annular grids with ”bad” stripes

The results of the WRRADPINN($\sin$) method modification on the annular region with banded excluded subareas are presented in Figure 10 and Table 8. The metrics were calculated on the original annular region without ”bad” strips. In Figure 10, part a) shows the original wavefront defined in the annular domain with the ”bad” band regions superimposed on it, part b) shows the original wavefront, part c) shows the reconstructed wavefront, and part d) shows the absolute deviation of the reconstructed wavefront from the original wavefront.

Method	MSE_N	δ_{perc}	SSIM
WRRADPINN(sin)	0.03169	1.68%	0.992

Table 8. WRRADPINN(sin) performance accuracy in the case of an annular region with ”bad” bands.

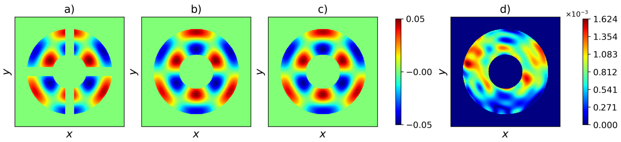

Figure 10. Result of wavefront reconstruction defined on a circular aperture with excluded band-like regions.

6.2 Irregular annular grid

The second type of irregular data considered was the set of points obtained from the experimental setup (Kopylov et al., 2024), on which a linear combination of Zernike polynomials $Z(2,0) - Z(4,0)$ was analytically specified and Poisson noise approximately 2% of the amplitude of the slopes was added to the slopes analytically calculated at the points. The results of the method on such a grid are presented in Figure 11 and show the recovery with a maximum deviation from the exact value of about 6.2% of the spread of the original signal amplitude.

It is important to note that unlike the regular grid case (with known slope values at 65,536 points), this configuration used a significantly coarser grid of just 144 points - several orders of magnitude smaller.

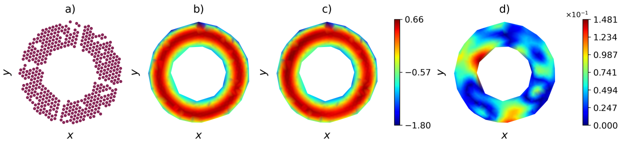

Figure 11. Result of wavefront reconstruction defined on the experimental set of 144 points.

In Figure 11, part a) shows the points of the annular domain with outer and inner radii of 0.5 and 1.03, respectively, where the slopes were set. Part b) shows the original wavefront set at the annular points depicted in part a), part c) shows the reconstructed wavefront obtained by WRRAPINN($\sin$). In part d), the absolute deviation of the reconstructed front from the original front is given.

The above presented results show the good performance of the proposed method both on an irregular annular aperture with excluded strip-like regions and on an irregular set of points 2 orders smaller than in the previously considered case of a regular grid.

7. Conclusion

The problem of front reconstruction by its slopes on regular and irregular grids is considered. Two modifications of the method based on physics-informed neural networks WRPINN and WRRADPINN are proposed for its solution, reducing the task to the problem of minimizing the mean-square deviation of the slopes of the sought nonlinear approximation from the registered values. The WRRADPINN modification with $\sin$ activation function has shown to be effective on rapidly oscillating wavefronts. Analysis of the method's performance on regular grids of smaller dimensionality, regular grids with ”bad” regions, and irregular grids has shown its efficiency with regard to the specifics of the considered data and promising for further analysis of the possibilities of its application in ophthalmology and the estimation of atmospheric turbulence parameters.

8. Acknowledgments

The results described in sections 2-3 were obtained by the first two authors with the financial support of the Ministry of Education and Science of the Russian Federation as part of the program of the Moscow Center for Fundamental and Applied Mathematics under the agreements № 075-15-2022-284, № 075-15-2025-345. The work described in sections 4-6 was obtained by all authors with the support of MSU Program of Development, Project No 23-SCH06-20.

References

Acevedo, C. H., Eshaghi, M., Dogariu, A., 2023. Propagation of asymmetric optical vortex beams through turbulence and evolution of their OAM spectra. *J. Opt. Soc. Am. A*, 40(12), 2135–2145.

Andreeva, M., Iroshnikov, N., Koryabin, A., Larichev, A., Shmalgauzen, V., 2012. Usage of wavefront sensor for estimation of atmospheric turbulence parameters. *Optoelectronics, Instrumentation and Data Processing*, 48, 197–204.

Baryshnikov, N., Denisov, D., Dzhumamuratova, A., Larichev, A., 2019. Development and research of an optoelectronic device based on a wavefront sensor to control the form parameters of intraocular lenses. *Measurement Techniques*, 62, 31–35.

Gbur, G., Tyson, R. K., 2008. Vortex beam propagation through atmospheric turbulence and topological charge conservation. *J. Opt. Soc. Am. A*, 25(1), 225–230.

Ge, X., Zhu, L., Gao, Z., Wang, N., Ye, H., Wang, S., Yang, P., 2023. Object-independent wavefront sensing method based on an unsupervised learning model for overcoming aberrations in optical systems. *Optics Letters*, 48(17), 4476–4479.

Goncharov, A., Iroshnikov, N., Larichev, A., Nikolaev, I., 2015. The impact of speckle on the measurement of eye aberrations. *Journal of Modern Optics*, 62(21), 1775–1780.

Grose, M., Schmidt, J. D., Hirakawa, K., 2024. Convolutional neural network for improved event-based Shack-Hartmann wavefront reconstruction. *Applied Optics*, 63(16), E35–E44.

Gu, H., Zhao, Z., Zhang, Z., Cao, S., Wu, J., Hu, L., 2021. High-precision wavefront reconstruction from Shack-Hartmann wavefront sensor data by a deep convolutional neural network. *Measurement Science and Technology*, 32(7), 075201.

He, Y., Liu, Z., Ning, Y., Li, J., Xu, X., Jiang, Z., 2021. Deep learning wavefront sensing method for Shack-Hartmann sensors with sparse sub-apertures. *Optics Express*, 29(11), 17669–17682.

Huang, J., Yao, L., Wu, S., Wang, G., 2023. Wavefront Reconstruction of Shack-Hartmann with Under-Sampling of Sub-Apertures. *Photonics*, 10, 65.

Hyde, M., Spencer, M., 2023. Spatiotemporal optical vortices in atmospheric turbulence. *Waves in Random and Complex Media*, 1–27.

Hyde, M. W., Porras, M. A., 2023. Propagation of spatiotemporal optical vortex beams in linear, second-order dispersive media. *Phys. Rev. A*, 108, 013519.

Kolodziejczyk, A., Bara, S., Jaroszewicz, Z., Sypek, M., 2007. The Light Sword Optical Element - a New Diffraction Structure with Extended Depth of Focus. *Journal of Modern Optics*, 37(8), 1283–1286.

Kopylov, E., Larichev, A., Iroshnikov, N., Sachkov, M., 2024. Project for the development of the adaptive optical system with Rayleigh LGS for the INASAN 2-meter telescope. K. J. Jackson, D. Schmidt, E. Vernet (eds), *Adaptive Optics Systems IX*, 13097, International Society for Optics and Photonics, SPIE, 1309738.

Kozlova, E. S., Savelyeva, A. A., Kadomina, E. A., Kotlyar, V. V., 2024. Study of the Influence of Turbulent Media on the Propagation of Squared Laguerre-Gaussian Beams. *Optical Memory and Neural Networks (Information Optics)*, 33(S2), S237–S248.

Larichev, A., Ivanov, P., Iroshnikov, N., Shmalhauzen, V., Otten, L., 2002. Adaptive system for eye-fundus imaging. *Quantum Electronics*, 32(10), 902–908.

Liu, S., Zhong, H., Li, Y., Liu, K., 2024. Fast and Highly Accurate Zonal Wavefront Reconstruction from Multi-Directional Slope and Curvature Information Using Subregion Cancelation. *Applied Sciences*, 14, 3476.

Ma, H., Zhang, W., Ning, X., Liu, H., Zhang, P., Zhang, J., 2023. Turbulence Aberration Restoration Based on Light Intensity Image Using GoogLeNet. *Photonics*, 10(3), 265.

Ning, Y., He, Y., Li, J., Sun, Q., Xi, F., Su, A., Yi, Y., Xu, X., 2024. Unsupervised learning-based wavefront sensing method for Hartmanns with insufficient sub-apertures. *Optics Continuum*, 3(2), 122–134.

Platt, B., Shack, R., 2001. History and principles of Shack–Hartmann wavefront sensing. *Journal of Refractive Surgery*, 17(5), S573–S577.

Raissi, M., Perdikaris, P., Karniadakis, G., 2019. Physics-informed neural networks: A deep learning framework for solving forward and inverse problems involving nonlinear partial differential equations. *Journal of Computational Physics*, 378, 686–707.

Razgulin, A., Iroshnikov, N., Larichev, A., Turganbaev, S., Romanenko, T., 2022. Estimates of the accuracy of the projection method with a fractional smoothness stabilizer in the problem of reconstructing the wavefront based on its slopes. *Differential Equations*, 58(7), 985–998.

Razgulin, A., Kuzhamaliyev, Y., Goncharov, A., Larichev, A., 2017. A variational method for wavefront reconstruction from Shack-Hartmann sensor measurements. *Atmospheric and Oceanic Optics*, 30(4), 399–403.

Razgulin, A., Kuzhamaliyev, Y., Iroshnikov, N., Larichev, A., 2019. A variational method of wavefront reconstruction from local slope measurements using a fractional order of smoothness stabilizer. *Computational Mathematics and Modeling*, 30(2), 164–176.

Romanenko, T., 2025. Wavefront PINN Recontstruction Method. https://github.com/TatianaRomanenko/WRPINN.git.

Wang, K., Song, L., Wang, C., Ren, Z., Zhao, G., Dou, J., Di, J., Barbastathis, G., Zhou, R., Zhao, J., Lam, E. Y., 2024. On the use of deep learning for phase recovery. *Light: Science & Applications*, 13(4), 13.

Wang, S., Cheng, M., Yang, X., Xu, J., Yang, Y., 2023. Self-focusing effect analysis of a perfect optical vortex beam in atmospheric turbulence. *Optics Express*, 31(13), 20861–20871.

Wang, S., Yu, X., Perdikaris, P., 2022. When and why PINNs fail to train: A neural tangent kernel perspective. *Journal of Computational Physics*, 449, 110768.

Wu, C., Zhu, M., Tan, Q., Kartha, Y., Lu, L., 2023a. A comprehensive study of non-adaptive and residual-based adaptive sampling for physics-informed neural networks. *Computer Methods in Applied Mechanics and Engineering*, 403, 115671.

Wu, J., Liang, J., Fei, S., Zhong, X., 2023b. Technique for Recovering Wavefront Phase Bad Points by Deep Learning. *Chinese Journal of Electronics*, 32(2), 303–312.

Zhang, Z., Jin, R., Chai, F., Lei, Z., Wen, L., Wang, S., Yang, P., 2024. Neural network algorithm for under-sampled wavefront reconstruction: mathematical analysis and implementation. *Optics Express*, 32(23), 41741–41756.

Zhao, M., Zhao, W., Wang, S., Yang, P., Yang, K., Lin, H., Kong, L., 2022. Centroid-Predicted Deep Neural Network in Shack-Hartmann Sensors. *IEEE Photonics Journal*, 14(1), 1-10.

Zheng, Y., Zhang, Y., Guo, L., Li, P., Wang, Z., Zhuang, Y., Lin, S., Tian, Y., Cai, Z., Huang, L., 2024. Neural network assisted high flexibility and high resolution Shack-Hartmann wavefront sensing for astronomical observation in darker sky areas. *Optics Express*, 32(15), 25676–25688.